



OPEN

Biaxial tensile behavior of stainless steel 316L manufactured by selective laser melting

Hao Wang^{1,2}, Xiaoyong Shu^{1,2}, Jianping Zhao^{1,2}✉ & I. V. Alexandrov³

In this study, miniaturized cruciform biaxial tensile specimens were optimized by finite element simulation software Ansys to vary five geometric parameters. The optimized specimens were utilized to characterize the biaxial tensile properties of 316L stainless steel fabricated through selective laser melting (SLM), with the two loading directions being vertical (X) and parallel (Y) to the building direction. It was discovered that at load ratios of 4:2 and 2:4, the yield strengths along X and Y orientations reached their respective maxima. By comparing the experimentally obtained yield loci against predictions by theoretical criteria including Mises, Hill48 and Hosford, it was found that the Hill48 anisotropic criterion corresponded most closely with the experimental results, while the other two criteria exhibited considerably larger deviations. Therefore, Hill48 was concluded to most accurately describe the yielding behaviors of SLM 316L under complex loading conditions.

Selective laser melting (SLM) is a powder bed additive manufacturing technology belonging to the category of powder bed fusion. It works by utilizing a high-power laser to selectively scan and melt the surface of metallic powder spread into a thin layer. This process is repeated layer-by-layer until the complete part is formed. SLM is capable of processing many metallic materials with high precision, directly fabricating complex components without the need for molds¹. In recent years, SLM has seen rapid development and been widely applied in aerospace², medical³, and automotive manufacturing. Compared with conventional methods, SLM technology can significantly reduce material waste, integrate design and manufacturing, enabling lightweight and customized fabrication of components.

316L stainless steel is one of the most widely processed metals by SLM, owing to its high corrosion resistance and excellent combination of strength and ductility after post-processing^{4,5}. Due to the excellent mechanical properties, corrosion resistance and biocompatibility of 316L stainless steel, SLM 316L can be used in medical device applications and orthopedic implants^{6,7}. Due to the design freedom provided by SLM and the excellent wear and corrosion resistance of 316L, SLM 316L is often used in the manufacture of furnace fixtures, heat exchange piping, turbine blades in jet engines, etc⁸.

However, differences between SLM and conventional manufacturing result in unique microstructures and mechanical anisotropy in SLM-processed 316L parts^{9,10}. In the horizontal direction parallel to the build layers, ultimate tensile strength (UTS) and elongation of SLM 316L have been reported to be up to 10% and 60% lower respectively than the vertical direction normal to the layers^{9,11,12}. This anisotropy is mainly attributed to the layer banding effects arising from localized remelting during SLM^{4,13,14}. Lack-of-fusion defects generated between layers also impart negative effects^{15,16}. In addition, rapid solidification and steep thermal gradients in SLM lead to fine cellular dendritic grains and elemental segregation along the build direction, which yield inferior tensile properties horizontally compared to vertically^{17–20}. Porosity defects and rough surfaces associated with partially fused powder particles also degrade the horizontal tensile behavior^{21–23}.

In summary, the intrinsic SLM process–structure–property relationships result in anisotropic tensile performance for 316L stainless steel. Further efforts are required to fundamentally understand the structure–property correlations, which will provide insights to guide SLM process optimization for balanced mechanical properties²⁴. Therefore, investigating the biaxial tensile properties of 316L fabricated by SLM is crucial.

Biaxial tensile testing of metallic materials provides critical insights into their forming limit diagrams (FLDs) and plastic deformation behaviors under complex strain paths^{25–27}. This is essential for predicting material formability and guiding the design of manufacturing processes for metallic parts²⁸. The cruciform specimen is one of

¹School of Mechanical and Power Engineering, Nanjing Tech University, Nanjing 211816, People's Republic of China. ²Institute of Reliability Centered Manufacturing (IRcM), Nanjing 211816, People's Republic of China. ³Department of Materials Science and Physics of Metals, Ufa University of Science and Technology, Ufa, Russia 450008. ✉email: jpzhaonjtech@163.com

the most commonly adopted sample geometries for biaxial tensile experiments due to its structural symmetry and relatively uniform stress state in the center gauge area^{29,30}. The dimensions of a cruciform specimen need to be carefully designed to achieve a balanced biaxial stress state during testing^{31–33}. Common design factors include the sample length, width, thickness, fillet radius, and length of gauge area. Proper dimension ratios have been analytically derived and experimentally validated to minimize undesirable stress concentrations for various materials^{31,34–36}. However, optimized geometries often have large volumes, which increases material waste. Therefore, this study utilizes finite element software Ansys to simulate biaxial tension experiments for designing miniaturized cruciform specimens and optimizing their geometric parameters.

Accurately predicting the yielding behaviors of metallic materials is essential for simulating their plastic deformation in manufacturing processes^{37,38}. The von Mises, Hill 1948 (Hill48) and Hosford yield criteria are among the most established anisotropic yield functions suitable for various metals^{39–43}. The von Mises criterion assumes that yielding occurs when the von Mises stress reaches a critical value, applicable for isotropic metals like mild steel⁴⁴. The Hill48 criterion introduces anisotropy by using different yield stresses along three material directions, providing good accuracy for cubic metals^{37,45}. The Hosford criterion generalizes the isotropic von Mises model with a tunable exponent parameter. The exponent value can be fitted to experimental data to capture anisotropic yielding. Compared to Hill48, Hosford yield surfaces have smoother corners better matching measured shapes. Two general yield criteria, isotropic Mises and anisotropic Hill48, are included in commercial nonlinear finite element software ABAQUS. The accuracy of the yield criterion can be verified by the results of biaxial tensile test.

In this study, miniaturized cruciform biaxial tensile specimens were designed and optimized by the finite element software Ansys. The biaxial mechanical behavior of SLM 316L was studied by the biaxial tensile test with the optimized miniaturized cruciform specimens, and the stress–strain curves under different load ratios were obtained. The yield loci of SLM 316L under biaxial stress is obtained by calculation. The yield loci obtained by experiments were compared with those calculated by Mises, Hill48 and Hosford yield criteria to verify the accuracy of different yield criteria. This can provide a reference for the numerical simulation to predict the performance of parts.

Specimens and methods

Design optimization of miniaturized cruciform specimens

To conduct biaxial tensile tests, cruciform specimens were designed using finite element analysis software ANSYS. Biaxial tensile simulations were performed to obtain the stress states of the specimens, based on which the geometries were optimized. Tensile tests employed cruciform specimens with overall dimensions shown in Fig. 1. Five geometric factors of the specimens were optimized, including thickness of the center gage section, width of the straight arm notches, length of the straight arm notches, number of notches, and fillet radius of the inner corner. The levels of each factor are listed in Table 1. Through iterative simulation and optimization, a cruciform specimen design inducing balanced biaxial stresses was obtained. The adopted specimen geometry

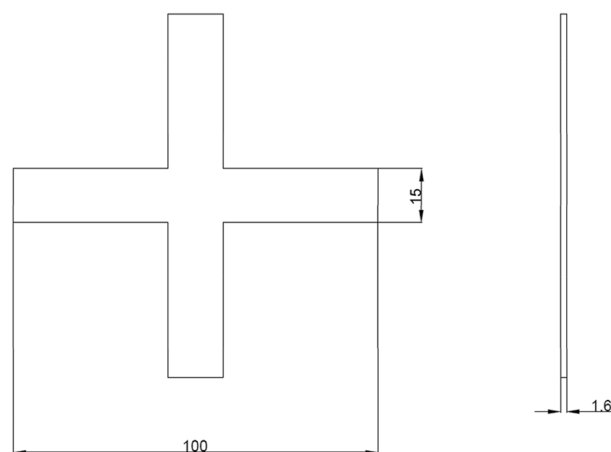


Figure 1. Basic dimensions of cruciform specimens.

	Thickness of the center gage section (mm)	Width of the straight arm notches (mm)	Length of the straight arm notches (mm)	Number of notches	Fillet radius of the inner corner (mm)
1	0.8	0.2	5	1	0.25
2	0.6	0.4	7.5	3	0.5
3	0.4	0.6	10	5	0.75
4	0.2	0.8	12.5	7	1

Table 1. Levels of geometric shape factors for cruciform specimens.

and dimensions enabled reliable characterization of the plastic deformation behavior through subsequent biaxial tensile experiments. A $L_{15}(4^5)$ orthogonal array was implemented for the orthogonal experimental design. Owing to the cruciform symmetry, only a quarter fraction was modeled for finite element analysis, as illustrated in Fig. 2 showing the FE model of the specimen.

Materials and additive manufacturing

The SLM process utilized a commercial gas-atomized 316L powder with particle size distribution shown in Table 2 and nominal composition listed in Table 3. Printing occurred under argon atmosphere to prevent oxidation. The adopted processing parameters are provided in Table 4. A reciprocating scanning strategy with 67° rotation between layers was implemented. The directly fabricated cruciform specimen by SLM is depicted in Fig. 3.

Biaxial tension testing

In situ biaxial tensile tests of SLM 316L cruciform specimens were performed using an IPBF-5000 system (CARE Measurement and Control Co., Tianjin, China). Full-field surface strain measurements were obtained through

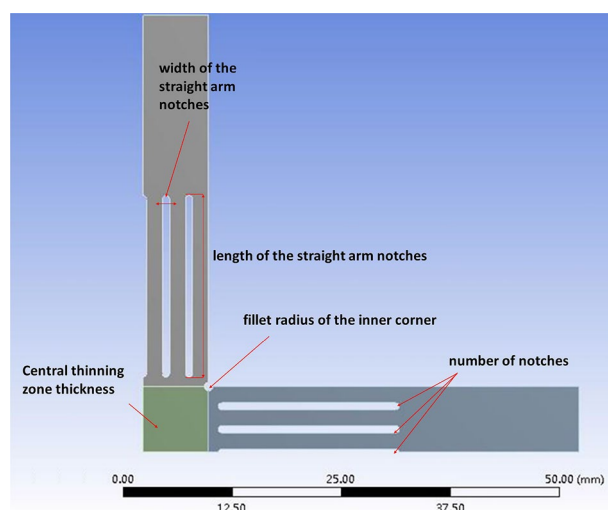


Figure 2. 1/4 Model of cruciform specimen.

Cumulative distribution (%)	Particle size (μm)
D10	20.22
D50	32.34
D90	51.84

Table 2. The particle size distribution of powder. D10, D50 and D90 refer to the particle size corresponding to the accumulative distribution of 10, 50 and 90%, respectively.

Element	Weight%
Fe	Balance
C	0.012
Si	0.690
Mn	1.260
P	0.010
S	0.007
Cr	16.470
Ni	12.720
Mo	2.440
O	0.062

Table 3. Chemical composition of 316L stainless steel powder.

Laser power (W)	400
Scanning speed (mm/s)	1300
Hatch distance (mm)	0.11
Powder layer thickness (mm)	0.06

Table 4. The processing parameters of SLM.

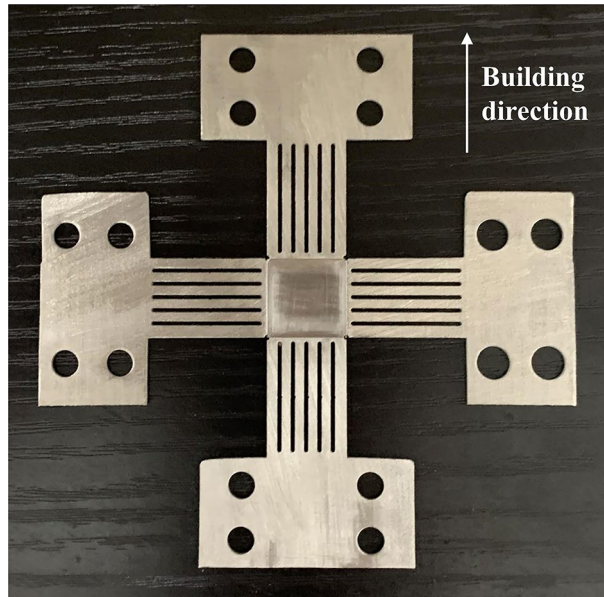


Figure 3. 316L cruciform specimens fabricated by SLM.

non-contact digital image correlation (DIC). Speckle patterns were applied on the gage sections (Fig. 4b). A FUJIFILM HF50SA-1 camera (FUJIFILM Holdings Corp., Tokyo, Japan) at 5 megapixel resolution and 9.7° angle captured speckle variations (Fig. 4a). Gaussian prefiltering and bicubic spline interpolation during post-processing reduced displacement measurement errors. The color scale depicts the DIC-determined minimum to maximum strains.

Load-controlled mode with fixed proportional $F_x : F_y$ tension loads was implemented, where X denotes vertical to the build direction, and Y parallel. Specific $F_x : F_y$ ratios were 4 : 0, 4 : 1, 4 : 2, 4 : 3, 4 : 4, 3 : 4, 2 : 4, 1 : 4, 0 : 4. Uniaxial tensile test values defined the 4:0 and 0:4 limits⁴⁶.

Ethical approval

This study did not involve human or animal subjects, and thus, no ethical approval was required. The study protocol adhered to the guidelines established by the journal.

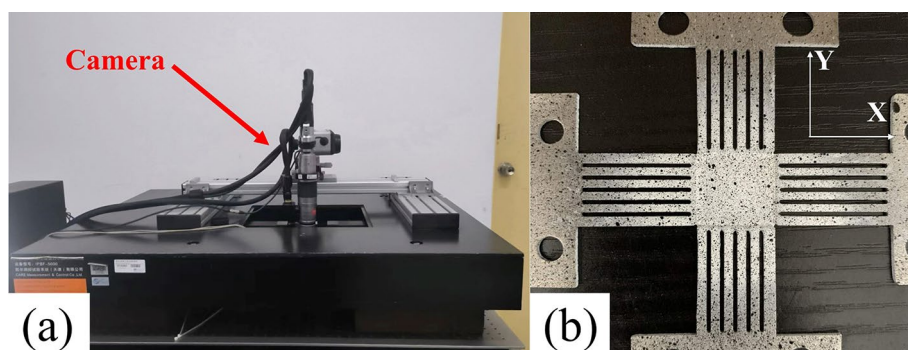


Figure 4. (a) DIC and biaxial tensile testing machine, (b) speckle pattern.

Results and discussion

Design optimization of miniaturized cruciform specimens

This study optimized the cruciform specimen geometry focusing on achieving uniform stress distribution in the center gage section. The stress uniformity γ of the center gage was defined as:

$$\gamma = \frac{1}{m} \sum_{i=1}^m \left(\frac{\sigma_{centre}^i}{\sigma_{mises}} \right)^2 \quad (1)$$

where m is the number of selected reference points ($m=6$, Fig. 5), and σ_{mises}^i is the von Mises stress at each reference node.

Figure 5 illustrates the schematic of the reference nodes.

Finite element models of cruciform specimens with dimensional variations per the factor levels in Table 1 and L15 orthogonal array were generated. Biaxial tensile simulations provided the stress states during loading. The stress uniformity γ was calculated using Eq. (1) based on the nodal stresses. Tables 5 and 6 list the computed γ values for node 1 stresses of 200 and 500 MPa, respectively. (Factors A, B, C, D, E in the table correspond to

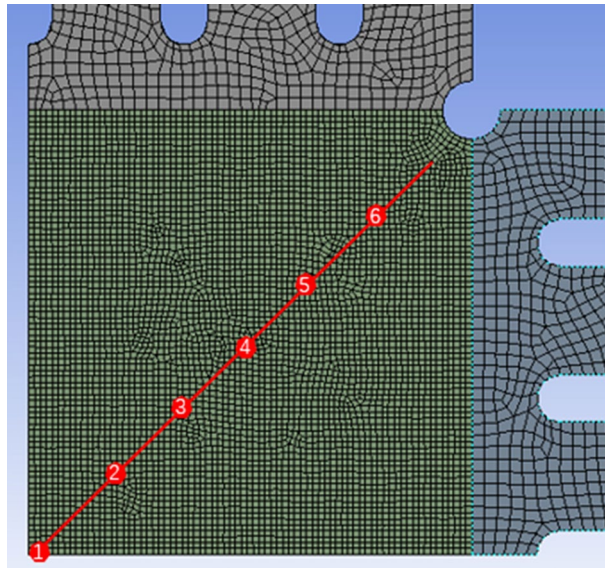


Figure 5. The schematic of the reference nodes.

Experiment number	Factor					Uniformity (γ)	Test scheme
	A	B	C	D	E		
1	1	1	1	1	1	1.050	$A_1 B_1 C_1 D_1 E_1$
2	1	2	2	2	2	1.054	$A_1 B_2 C_2 D_2 E_2$
3	1	3	3	3	3	1.066	$A_1 B_3 C_3 D_3 E_3$
4	1	4	4	4	4	1.088	$A_1 B_4 C_4 D_4 E_4$
5	2	1	2	3	4	1.075	$A_2 B_1 C_2 D_3 E_4$
6	2	2	1	4	3	1.066	$A_2 B_2 C_1 D_4 E_3$
7	2	3	4	1	2	1.065	$A_2 B_3 C_4 D_1 E_2$
8	2	4	3	2	1	1.048	$A_2 B_4 C_3 D_2 E_1$
9	3	1	3	4	2	1.066	$A_3 B_1 C_3 D_4 E_2$
10	3	2	1	3	1	1.063	$A_3 B_2 C_1 D_3 E_1$
11	3	3	4	2	4	1.092	$A_3 B_3 C_4 D_2 E_4$
12	3	4	2	1	3	1.085	$A_3 B_4 C_2 D_1 E_3$
13	4	1	4	2	3	1.099	$A_4 B_1 C_4 D_2 E_3$
14	4	2	3	1	4	1.104	$A_4 B_2 C_3 D_1 E_4$
15	4	3	2	4	1	1.082	$A_4 B_3 C_2 D_4 E_1$
16	4	4	1	3	2	1.092	$A_4 B_4 C_1 D_3 E_2$

Table 5. Orthogonal array and results ($\sigma_{mises}^1 = 200$ MPa).

Experiment number	Factor					Uniformity (γ)	Test scheme
	A	B	C	D	E		
1	1	1	1	1	1	1.017	$A_1B_1C_1D_1E_1$
2	1	2	2	2	2	1.018	$A_1B_2C_2D_2E_2$
3	1	3	3	3	3	1.020	$A_1B_3C_3D_3E_3$
4	1	4	4	4	4	1.022	$A_1B_4C_4D_4E_4$
5	2	1	2	3	4	1.020	$A_2B_1C_2D_3E_4$
6	2	2	1	4	3	1.019	$A_2B_2C_1D_4E_3$
7	2	3	4	1	2	1.018	$A_2B_3C_4D_1E_2$
8	2	4	3	2	1	1.017	$A_2B_4C_3D_2E_1$
9	3	1	3	4	2	1.018	$A_3B_1C_3D_4E_2$
10	3	2	1	3	1	1.015	$A_3B_2C_1D_3E_1$
11	3	3	4	2	4	1.019	$A_3B_3C_4D_2E_4$
12	3	4	2	1	3	1.018	$A_3B_4C_2D_1E_3$
13	4	1	4	2	3	1.020	$A_4B_1C_4D_2E_3$
14	4	2	3	1	4	1.019	$A_4B_2C_3D_1E_4$
15	4	3	2	4	1	1.017	$A_4B_3C_2D_4E_1$
16	4	4	1	3	2	1.017	$A_4B_4C_1D_3E_2$

Table 6. Orthogonal array and results ($\sigma_{mises}^1 = 500$ MPa).

the thickness of the center gage section, width of the straight arm notches, length of the straight arm notches, number of notches and fillet radius of the inner corner respectively).

The influence of each factor on γ was determined using the Statistica software based on the computed results in Tables 5 and 6, as depicted in Figs. 6 and 7.

Figure 6 indicates geometry $A_2B_2C_3D_2E_1$ conferring optimal γ under 200 MPa, while Fig. 7 shows geometry $A_3B_2C_2D_1E_1$ being optimal for 500 MPa. Although one notch (D_1) minimally influenced γ at 500 MPa, it exceeded the average effect at 200 MPa. Similarly, three notches (D_2) also surpassed the mean impact on γ at

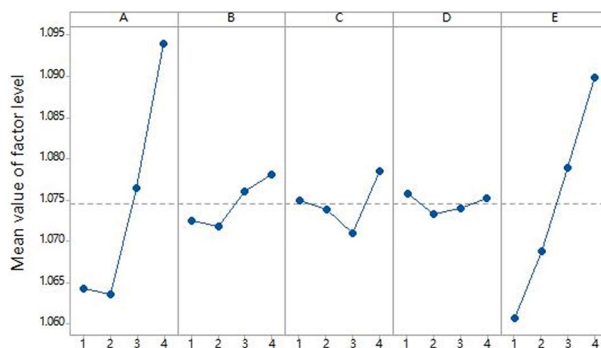


Figure 6. Influence of factor levels on uniformity(200 MPa).

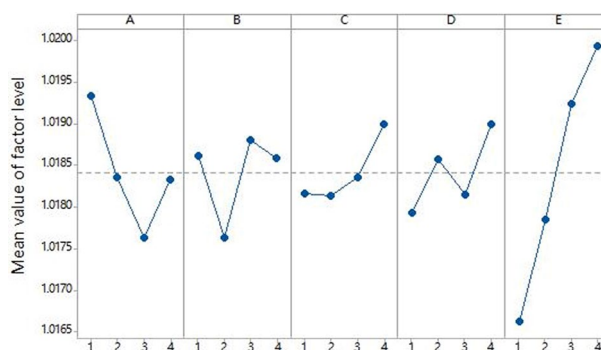


Figure 7. Influence of factor levels on uniformity(500 MPa).

500 MPa. In contrast, five notches (D_3) exhibited relatively low effects at both stresses. Hence, five notches (D_3) were chosen for the notch number. Considering diminished formability with excessively small fillet radius, 0.25 mm (E_1) was replaced with 0.5 mm (E_2). Likewise, the notch width was increased from 0.4 mm (B_2) to 0.8 mm (B_4). Integrating these factors, geometry $A_3B_4C_3D_3E_2$ was selected as the optimum cruciform design, with final dimensions listed in Table 7.

True stress-true strain curves for different loading ratios

To obtain the true stress-true strain curves under nine loading ratios, the area of the mid-plane cross-section in the gage region was defined as S , calculated by:

$$S = w \cdot t = \frac{w_0 \cdot t_0 \cdot l_0}{l} = \frac{w_0 \cdot t_0}{1 + \varepsilon} \quad (2)$$

where l_0 , w_0 , t_0 are the initial length, width and thickness of the gage section. l , w , t represent the instantaneous counterparts, and ε is the strain along the measurement direction perpendicular to the cross-sectional area S . The true stress σ can then be expressed as:

$$\sigma = \frac{F}{S} \quad (3)$$

Figure 8 presents the true stress-true strain curves of SLM 316L stainless steel under nine biaxial tension loading ratios. The flow behavior varied with the stress state, and the strain hardening exponent increased as the load ratio shifted from uniaxial toward balanced biaxial tension. Table 8 lists the yield strengths along the two directions under various loading ratios. Figure 9 presents the evolution of yield strengths along the two directions with varying loading ratios. The peaks were attained at 4:2 and 2:4 ratios for the respective orientations, differing from conventionally forged 316L that typically peaks at equivalent ratios⁴⁷.

Experimental yield locus

To determine the yield points for the tensile tests, true plastic strains ε_x^p and ε_y^p along the X and Y orientations were calculated using Eq. (4).

$$\varepsilon_x^p = \varepsilon_x - \frac{\sigma_x}{C_x}; \varepsilon_y^p = \varepsilon_y - \frac{\sigma_y}{C_y} \quad (4)$$

where C_x and C_y are the slopes of the elastic portions of curves $\varepsilon_x - \sigma_x$ and $\varepsilon_y - \sigma_y$ measured in MPa from the biaxial tensile tests. ε_x and ε_y represent the true strains along the X and Y orientations, respectively.

For simplicity, plastic work contours are often considered equivalent to experimentally measured yield point trajectories⁴⁸. Uniaxial tensile tests on SLM 316L vertical to the build direction using ASTM E8 specimens provided uniaxial true stresses σ_0^p corresponding to plastic strains ε_0^p of 0.002, 0.006 and 0.01. The plastic work W was measured per unit of plastic strain ε_0^p . In biaxial tensile tests with fixed stress ratios, the sum of plastic work along both orientations was obtained. Equivalent yield loci were identified when the unit plastic works W were equal under different stress states. For instance, as depicted in Fig. 10, point $(\sigma_1^{p*}, \sigma_2^{p*})$ represents a given biaxial tension stress state⁴⁹. Point $(\bar{\sigma}^*, \bar{\varepsilon}^{p*})$ refers to the uniaxial stress-strain curve vertical to the building direction, satisfying:

$$\int_0^{\sigma_1^{p*}} \sigma_1 d\varepsilon_1^p + \int_0^{\sigma_2^{p*}} \sigma_2 d\varepsilon_2^p = \int_0^{\bar{\varepsilon}^{p*}} \bar{\sigma} d\bar{\varepsilon}^p \quad (5)$$

Notably, the integration in Eq. (5) was performed using discrete numerical integration, specifically integrating discrete trapezoidal areas encompassed by the data points and horizontal axis. This method yielded yield loci at three equivalent plastic strain levels for SLM 316L, as depicted in Fig. 11.

The yield contours demonstrate similar evolving trends in shape and size with increasing plastic deformation. Per the convexity principle, the plastic work contours expand outwards. Owing to strain hardening, the contours intensify from center to periphery at a given plastic strain increment. Notably, anisotropic mechanical properties induced asymmetry in the yield locus shapes along the balanced biaxial tension path, deviating from classic isotropic predictions. This signifies that deformation history and direction dependency in the SLM-processed 316L stainless steel influence yielding even at relatively small strains. The expanded yield area indicates enhanced formability, but the asymmetric distortions suggest potentially complex yielding characteristics under multi-axial loading.

	The thickness of the center gage section (mm)	Width of the straight arm notches (mm)	Length of the straight arm notches (mm)	The number of notches	Fillet radius of the inner corner (mm)
Optimal geometry	0.4	0.8	10	5	0.5

Table 7. Optimal geometry of cruciform specimens.

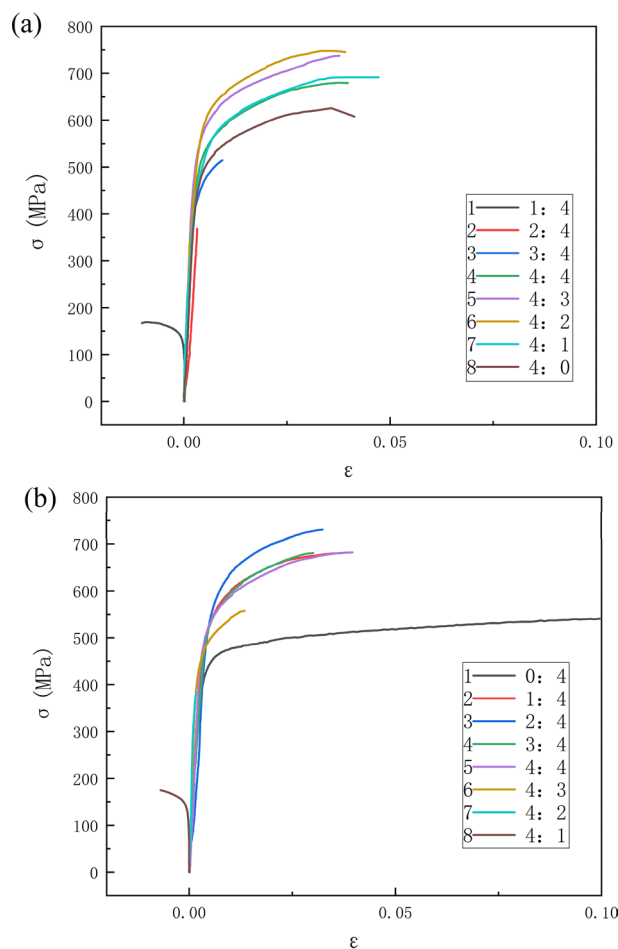


Figure 8. True stress-true strain curve of SLM 316L for different loading ratios, (a) X direction, (b) Y direction.

Testing direction	Load ratio (X/Y)	Yield strength at X (MPa)	Yield strength at Y (MPa)
Uniaxial	0:4		500.3
Biaxial	1:4		543.2
Biaxial	2:4		588.4
Biaxial	3:4	399.8	563.6
Biaxial	4:4	509.1	509.2
Biaxial	4:3	558.4	418.5
Biaxial	4:2	582.5	
Biaxial	4:1	550.2	
Uniaxial	4:0	499.7	

Table 8. Biaxial tensile tests data at various load ratios.

Comparison and analysis of experimental and theoretical locus

This section compares the experimentally obtained yield loci against predictions by theoretical yield criteria (Mises, Hill48, Hosford). The calculation of the parameters in theoretical yield criterion is adequately elaborated in Refs.^{40,43}. To quantify the correspondence between the calculated and measured yield points, the mean error δ was defined as an accuracy metric:

$$\delta = \frac{1}{n} \sum_{i=1}^n \frac{d_i}{\sqrt{(\sigma_1^i)^2 + (\sigma_2^i)^2}} \tag{6}$$

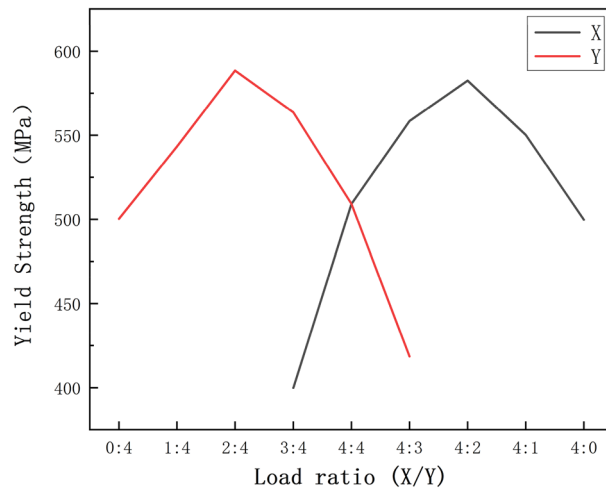


Figure 9. Evolution of yield strength with loading ratios.

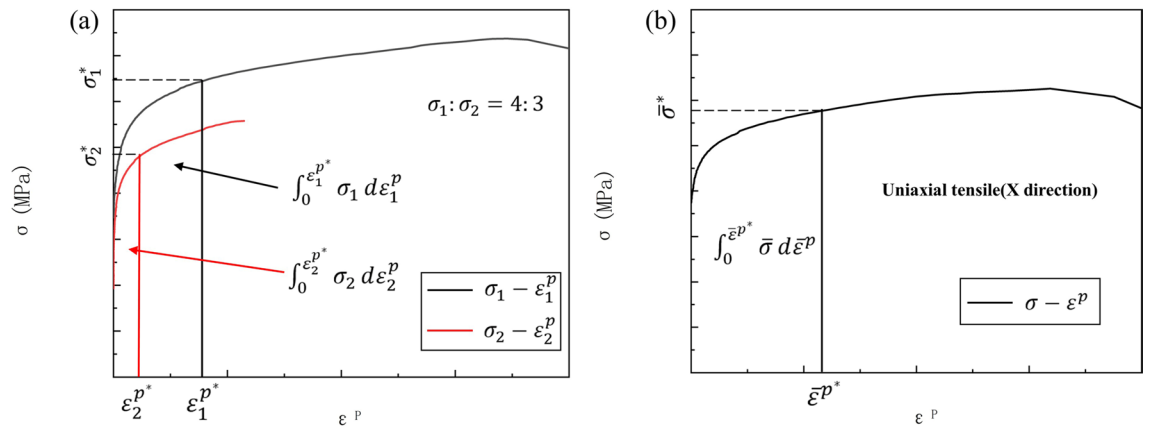


Figure 10. Determination procedures of plastic work contours. (a) Biaxial tensile condition; (b) uniaxial tensile condition.

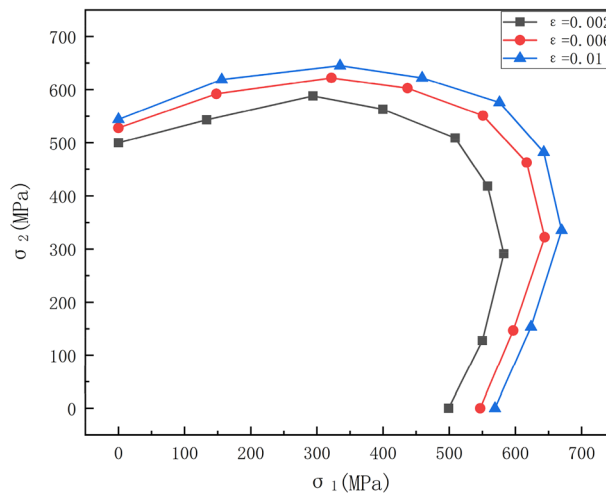


Figure 11. The experimental yield locus of SLM 316L at equivalent plastic strain 0.2, 0.6 and 1%.

where (σ_1^i, σ_2^i) denotes the experimental yield point coordinates, d_i is the normal distance from the point to the calculated yield contour, and n is the number of experimental points. Figure 12 presents the measured yield loci versus those predicted by theoretical criteria. Figure 13 shows the mean errors between experimental and calculated values.

As shown in Fig. 12, the Hosford yield criteria deviated considerably from experiments under 4:2 and 2:4 loading ratios, with significant inaccuracies in balanced biaxial tension prediction. The Hosford yield criteria, grounded in crystalline plasticity principles, precludes shear stress components in its formulation. However, SLM 316L stainless steel possesses intricate grain morphological distributions, which the limited anisotropy

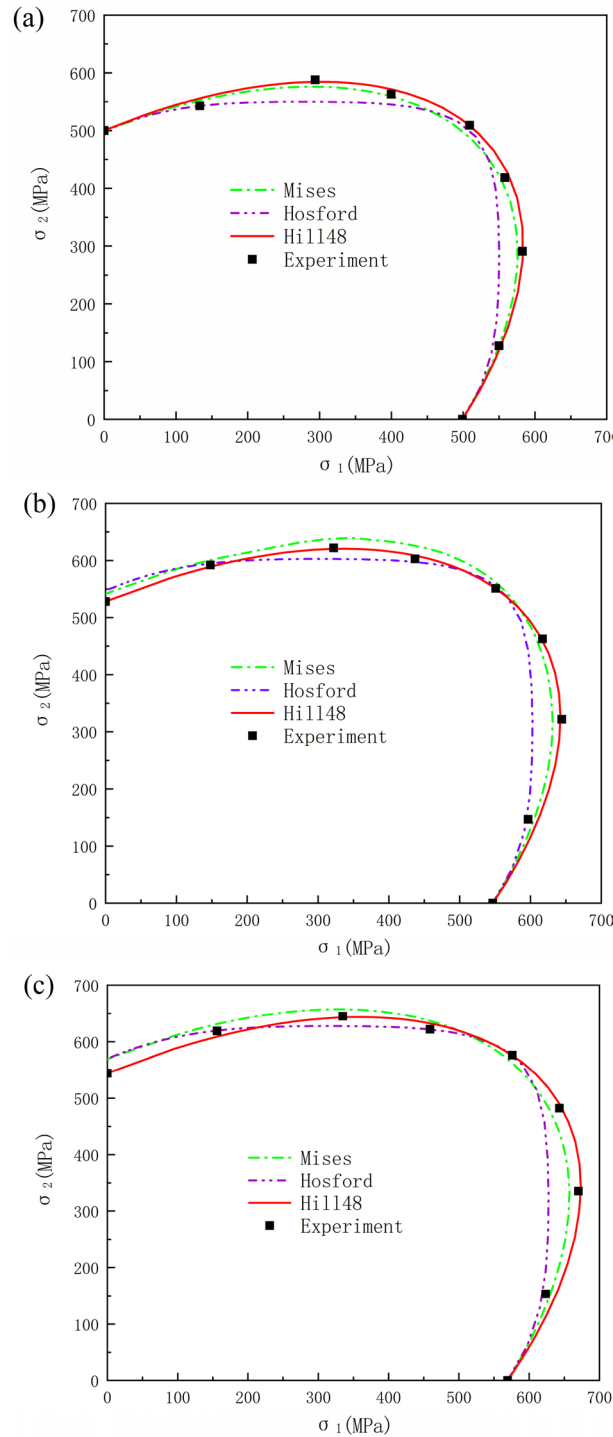


Figure 12. Comparison between experimental and calculated yield loci. (a) $\epsilon_0^p = 0.002$, (b) $\epsilon_0^p = 0.006$, (c) $\epsilon_0^p = 0.01$.

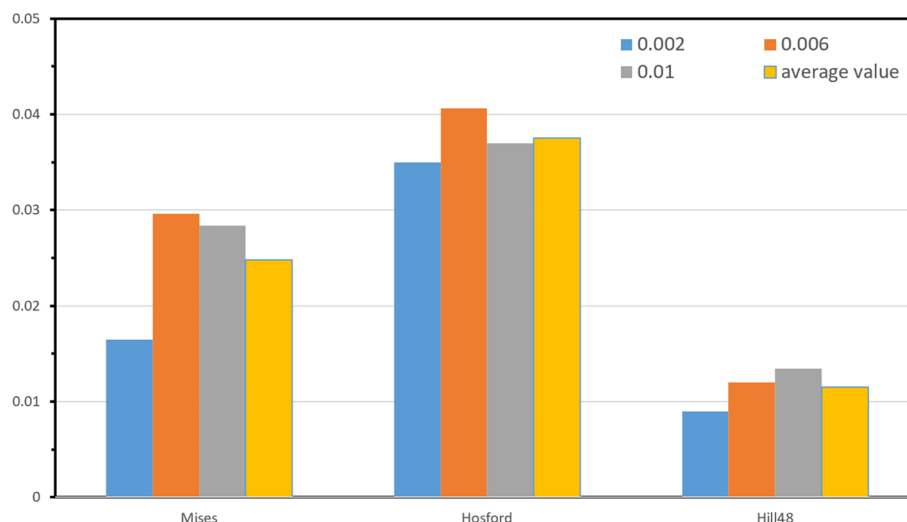


Figure 13. The mean errors between experimental and calculated values.

parameters in the Hosford yield criteria struggle to fully delineate. Additionally, the Hosford criterion does not incorporate shear stresses, that notably sway yielding responses of anisotropic alloys under complex loading states. This underpins appreciable deviations between Hosford-predicted and experimentally observed yield loci, especially for biaxial tension conditions, in the SLM 316L alloy. Although the Mises criterion exhibited moderately improved alignment with experimental yield loci, its inherent isotropy prevented capturing the experimentally observed yield contour asymmetry induced by the anisotropic behavior of SLM 316L. Consequently, inadequate conformance persisted between the symmetric Mises predictions and the asymmetric measured yield loci. Comparatively, the Hill48 contour aligned closely with experiments, which Fig. 13 quantifies. The Hosford criterion had the largest mean error versus experiments, while the Hill48 error was markedly lower than the other two models. As a phenomenological criterion on the macroscale, the Hill48 yield criteria can delineate the yielding behavior of materials with intricate grain distributions, like SLM 316L stainless steel, with relatively high accuracy despite only using a limited set of anisotropy parameters. Therefore, Hill48 is more suitable for describing the multi-axis yield behavior of SLM 316L. Moreover, all criteria showed increased deviations at higher versus lower strains per Fig. 13.

Summary and conclusions

In this work, biaxial tension simulations were conducted via Ansys to optimize the dimensional parameters of miniaturized cruciform specimens. The optimized samples were then fabricated from 316L stainless steel by SLM, and experimentally tested under biaxial loading to characterize the mechanical performance. Their yield loci obtained computationally were benchmarked against loci predicted by theoretical yield criteria. The key conclusions are:

1. The biaxial stress–strain response of SLM 316L stainless steel was loading-ratio-dependent, with the yield strengths along the two orientations reaching respective maxima at 4:2 and 2:4 ratios.
2. Adhering to the concept of plastic work contours, the yield loci of SLM 316L were obtained through computations. It was revealed that with increasing plastic deformation, the yield loci expanded outwards following the convexity principle. Moreover, asymmetry became evident in the calculated yield contours, attributed to the inherent anisotropy of 316L fabricated by selective laser melting.
3. Comparisons between experimentally obtained yield loci and model predictions based on Mises, Hill48 and Hosford criteria reveal the Hill48 anisotropic function as most accurately capturing the measured yielding behavior of SLM 316L under complex loading. The other two criteria deviated considerably from experiments. Thus, the Hill48 anisotropic criterion optimally delineates the anisotropic yield characteristics of additively manufactured 316L stainless steel.

Data availability

Data will be made available on request (Hao Wang: wh_njtech@163.com).

Received: 24 August 2023; Accepted: 8 December 2023

Published online: 11 December 2023

References

1. Gu, D. D., Meiners, W., Wissenbach, K. & Poprawe, R. Laser additive manufacturing of metallic components: Materials, processes and mechanisms. *Int. Mater. Rev.* **57**, 133–164. <https://doi.org/10.1179/1743280411y.0000000014> (2012).

2. Li, P., Warner, D. H., Fatemi, A. & Phan, N. Critical assessment of the fatigue performance of additively manufactured Ti-6Al-4V and perspective for future research. *Int. J. Fatigue* **85**, 130–143. <https://doi.org/10.1016/j.ijfatigue.2015.12.003> (2016).
3. Kohal, R. J. *et al.* Custom-made root analogue titanium implants placed into extraction sockets—An experimental study in monkeys. *Clin. Oral Implants Res.* **8**, 386–392. <https://doi.org/10.1034/j.1600-0501.1997.080505.x> (1997).
4. Prashanth, K. G. *et al.* Microstructure and mechanical properties of Al-12Si produced by selective laser melting: Effect of heat treatment. *Mater. Sci. Eng. A* **590**, 153–160. <https://doi.org/10.1016/j.msea.2013.10.023> (2014).
5. Zhong, Y., Liu, L., Wilkman, S., Cui, D. & Shen, Z. Intragranular cellular segregation network structure strengthening 316L stainless steel prepared by selective laser melting. *J. Nucl. Mater.* **470**, 170–178. <https://doi.org/10.1016/j.jnucmat.2015.12.034> (2016).
6. Pothala, S. & Jagannadha Raju, M. V. Recent advances of metallic bio-materials in additive manufacturing in biomedical implants—A review. *Mater. Today Proc.* <https://doi.org/10.1016/j.matpr.2023.07.109> (2023).
7. Nabeel, M. *et al.* Comparison of the properties of additively manufactured 316L stainless steel for orthopedic applications: A review. *World Sci. Annu. Rev. Funct. Mater.* **1**, 2230001. <https://doi.org/10.1142/s281092282230001x> (2023).
8. Yap, C. Y. *et al.* Review of selective laser melting: Materials and applications. *Appl. Phys. Rev.* <https://doi.org/10.1063/1.4935926> (2015).
9. Spierings, A. B., Starr, T. L. & Wegener, K. Fatigue performance of additive manufactured metallic parts. *Rapid Prototyp. J.* **19**, 88–94. <https://doi.org/10.1108/13552541311302932> (2013).
10. Casati, R., Lemke, J. & Vedani, M. Microstructure and fracture behavior of 316L austenitic stainless steel produced by selective laser melting. *J. Mater. Sci. Technol.* **32**, 738–744. <https://doi.org/10.1016/j.jmst.2016.06.016> (2016).
11. Riemer, A. *et al.* On the fatigue crack growth behavior in 316L stainless steel manufactured by selective laser melting. *Eng. Fract. Mech.* **120**, 15–25. <https://doi.org/10.1016/j.engfracmech.2014.03.008> (2014).
12. Cherry, J. A. *et al.* Investigation into the effect of process parameters on microstructural and physical properties of 316L stainless steel parts by selective laser melting. *Int. J. Adv. Manuf. Technol.* **76**, 869–879. <https://doi.org/10.1007/s00170-014-6297-2> (2015).
13. Kruth, J. P., Levy, G., Klocke, F. & Childs, T. H. C. Consolidation phenomena in laser and powder-bed based layered manufacturing. *CIRP Ann.* **56**, 730–759. <https://doi.org/10.1016/j.cirp.2007.10.004> (2007).
14. Thijs, L., Kempen, K., Kruth, J.-P. & Van Humbeeck, J. Fine-structured aluminium products with controllable texture by selective laser melting of pre-alloyed AlSi10Mg powder. *Acta Mater.* **61**, 1809–1819. <https://doi.org/10.1016/j.actamat.2012.11.052> (2013).
15. Aboulkhair, N. T., Maskery, L., Tuck, C., Ashcroft, I. & Everitt, N. M. On the formation of AlSi10Mg single tracks and layers in selective laser melting: Microstructure and nano-mechanical properties. *J. Mater. Process. Technol.* **230**, 88–98. <https://doi.org/10.1016/j.jmatprotec.2015.11.016> (2016).
16. Liu, F. *et al.* Microstructure and residual stress of laser rapid formed Inconel 718 nickel-base superalloy. *Opt. Laser Technol.* **43**, 208–213. <https://doi.org/10.1016/j.optlastec.2010.06.015> (2011).
17. Gu, D. & Shen, Y. Processing conditions and microstructural features of porous 316L stainless steel components by DMLS. *Appl. Surf. Sci.* **255**, 1880–1887. <https://doi.org/10.1016/j.apsusc.2008.06.118> (2008).
18. Santos, E. C., Shiomi, M., Osakada, K. & Laoui, T. Rapid manufacturing of metal components by laser forming. *Int. J. Mach. Tools Manuf.* **46**, 1459–1468. <https://doi.org/10.1016/j.ijmactools.2005.09.005> (2006).
19. Frazier, W. E. Metal additive manufacturing: A review. *J. Mater. Eng. Perform.* **23**, 1917–1928. <https://doi.org/10.1007/s11665-014-0958-z> (2014).
20. Herzog, D., Seyda, V., Wycisk, E. & Emmelmann, C. Additive manufacturing of metals. *Acta Mater.* **117**, 371–392. <https://doi.org/10.1016/j.actamat.2016.07.019> (2016).
21. Kruth, J.-P., Deckers, J., Yasa, E. & Wauthle, R. Assessing and comparing influencing factors of residual stresses in selective laser melting using a novel analysis method. *Proc. Inst. Mech. Eng. Part B J. Eng. Manuf.* **226**, 980–991. <https://doi.org/10.1177/0954405412437085> (2012).
22. Shiomi, M., Osakada, K., Nakamura, K., Yamashita, T. & Abe, F. Residual stress within metallic model made by selective laser melting process. *CIRP Ann.* **53**, 195–198. [https://doi.org/10.1016/S0007-8506\(07\)60677-5](https://doi.org/10.1016/S0007-8506(07)60677-5) (2004).
23. Mercelis, P. & Kruth, J.-P. Residual stresses in selective laser sintering and selective laser melting. *Rapid Prototyp. J.* **12**, 254–265. <https://doi.org/10.1108/13552540610707013> (2006).
24. Van Bael, S. *et al.* Micro-CT-based improvement of geometrical and mechanical controllability of selective laser melted Ti6Al4V porous structures. *Mater. Sci. Eng. A* **528**, 7423–7431. <https://doi.org/10.1016/j.msea.2011.06.045> (2011).
25. Kuwabara, T. Advances in experiments on metal sheets and tubes in support of constitutive modeling and forming simulations. *Int. J. Plast.* **23**, 385–419. <https://doi.org/10.1016/j.ijplas.2006.06.003> (2007).
26. Tasan, C. C., Hoefnagels, J. P. M., ten Horn, C. H. L. J. & Geers, M. G. D. Experimental analysis of strain path dependent ductile damage mechanics and forming limits. *Mech. Mater.* **41**, 1264–1276. <https://doi.org/10.1016/j.mechmat.2009.08.003> (2009).
27. Yoon, J.-W., Barlat, F., Dick, R. E., Chung, K. & Kang, T. J. Plane stress yield function for aluminum alloy sheets—part II: FE formulation and its implementation. *Int. J. Plast.* **20**, 495–522. [https://doi.org/10.1016/S0749-6419\(03\)00099-8](https://doi.org/10.1016/S0749-6419(03)00099-8) (2004).
28. Zhang, C., Leotoing, L., Guines, D. & Ragneau, E. Theoretical and numerical study of strain rate influence on AA5083 formability. *J. Mater. Process. Technol.* **209**, 3849–3858. <https://doi.org/10.1016/j.jmatprotec.2008.09.003> (2009).
29. Kuwabara, T., Van Bael, A. & Iizuka, E. Measurement and analysis of yield locus and work hardening characteristics of steel sheets with different r-values. *Acta Mater.* **50**, 3717–3729. [https://doi.org/10.1016/S1359-6454\(02\)00184-2](https://doi.org/10.1016/S1359-6454(02)00184-2) (2002).
30. Abu-Farha, H., Hector, L. G. & Khraisheh, M. Cruciform-shaped specimens for elevated temperature biaxial testing of lightweight materials. *JOM* **1989**(61), 48–56. <https://doi.org/10.1007/s11837-009-0121-8> (2009).
31. Kuwabara, T., Yoshida, K., Narihara, K. & Takahashi, S. Anisotropic plastic deformation of extruded aluminum alloy tube under axial forces and internal pressure. *Int. J. Plast.* **21**, 101–117. <https://doi.org/10.1016/j.ijplas.2004.04.006> (2005).
32. Xiao, R. A review of cruciform biaxial tensile testing of sheet metals. *Exp. Tech.* **43**, 501–520. <https://doi.org/10.1007/s40799-018-00297-6> (2019).
33. Dunand, M. & Mohr, D. Hybrid experimental–numerical analysis of basic ductile fracture experiments for sheet metals. *Int. J. Solids Struct.* **47**, 1130–1143. <https://doi.org/10.1016/j.ijsolstr.2009.12.011> (2010).
34. Lamkanfi, E., Van Paepegem, W. & Degrieck, J. Shape optimization of a cruciform geometry for biaxial testing of polymers. *Polym. Test.* **41**, 7–16. <https://doi.org/10.1016/j.polymertesting.2014.09.016> (2015).
35. Koç, M., Billur, E. & Cora, Ö. N. An experimental study on the comparative assessment of hydraulic bulge test analysis methods. *Mater. Des.* **32**, 272–281. <https://doi.org/10.1016/j.matdes.2010.05.057> (2011).
36. Lee, M.-G., Kim, D., Kim, C., Wenner, M. L. & Chung, K. Spring-back evaluation of automotive sheets based on isotropic–kinematic hardening laws and non-quadratic anisotropic yield functions, part III: Applications. *Int. J. Plast.* **21**, 915–953. <https://doi.org/10.1016/j.ijplas.2004.05.014> (2005).
37. Taherizadeh, A., Green, D. E., Ghaei, A. & Yoon, J.-W. A non-associated constitutive model with mixed iso-kinematic hardening for finite element simulation of sheet metal forming. *Int. J. Plast.* **26**, 288–309. <https://doi.org/10.1016/j.ijplas.2009.07.003> (2010).
38. Tardif, N. & Kyriakides, S. Determination of anisotropy and material hardening for aluminum sheet metal. *Int. J. Solids Struct.* **49**, 3496–3506. <https://doi.org/10.1016/j.ijsolstr.2012.01.011> (2012).
39. Banabic, D. *Sheet Metal Forming Processes: Constitutive Modelling and Numerical Simulation* 1st edn. (Springer-Verlag, 2009).
40. Hosford, W. F. A generalized isotropic yield criterion. *J. Appl. Mech.* **39**, 607–609. <https://doi.org/10.1115/1.3422732> (1972).
41. Banabic, D., Bunge, H. J., Pöhlant, K. & Tekkaya, A. E. *Formability of Metallic Materials: Plastic Anisotropy, Formability Testing, Forming Limits* (Springer, 2000).

42. Bouvier, S., Gardey, B., Haddadi, H. & Teodosiu, C. Characterization of the strain-induced plastic anisotropy of rolled sheets by using sequences of simple shear and uniaxial tensile tests. *J. Mater. Process. Technol.* **174**, 115–126. <https://doi.org/10.1016/j.jmatp.rotec.2005.04.086> (2006).
43. Hill, R. A theory of the yielding and plastic flow of anisotropic metals. *Proc. R. Soc. Lond. Ser. A Math. Phys. Sci.* **193**, 281–297. <https://doi.org/10.1098/rspa.1948.0045> (1948).
44. Khan, A. S. & Liu, H. Strain rate and temperature dependent fracture criteria for isotropic and anisotropic metals. *Int. J. Plast.* **37**, 1–15. <https://doi.org/10.1016/j.ijplas.2012.01.012> (2012).
45. Kim, S. B., Huh, H., Bok, H. H. & Moon, M. B. Forming limit diagram of auto-body steel sheets for high-speed sheet metal forming. *J. Mater. Process. Technol.* **211**, 851–862. <https://doi.org/10.1016/j.jmatp.rotec.2010.01.006> (2011).
46. Zhang, W., Zhu, Z., Zhou, C. & He, X. Biaxial tensile behavior of commercially pure titanium under various in-plane load ratios and strain rates. *Metals* **11**, 1–18. <https://doi.org/10.3390/met11010155> (2021).
47. Hu, Y., Chen, J. & Wang, B. Global nonequilibrium energy criterion for predicting strength of 316L stainless steel under complex loadings: Theoretical modeling and experimental validation. *Sci. China Phys. Mech. Astron.* **65**, 244611. <https://doi.org/10.1007/s11433-021-1850-0> (2022).
48. Kuwabara, T. & Nakajima, T. Material modeling of 980 MPa dual phase steel sheet based on biaxial tensile test and in-plane stress reversal test. *J. Solid Mech. Mater. Eng.* **5**, 709–720. <https://doi.org/10.1299/jmmp.5.709> (2011).
49. Hou, Z. *et al.* Biaxial tensile behavior and yield loci of dual-phase steel sheets. *J. Iron Steel Res. Int.* **25**, 589–597. <https://doi.org/10.1007/s42243-018-0074-7> (2018).

Acknowledgements

This research was supported by The National Key Research and Development Program of China (2021YFC3001804).

Author contributions

H.W.: Writing-Original Draft, Validation, Formal analysis, Visualization, Investigation, Conceptualization, Data Curation. X.S.: Data Curation, Investigation, Formal analysis. J.Z.: Methodology, Writing-Review & Editing, Funding acquisition, Resources, Supervision, Project administration. I.V. A.: Writing-Review & Editing.

Competing interests

The authors declare no competing interests.

Additional information

Correspondence and requests for materials should be addressed to J.Z.

Reprints and permissions information is available at www.nature.com/reprints.

Publisher's note Springer Nature remains neutral with regard to jurisdictional claims in published maps and institutional affiliations.



Open Access This article is licensed under a Creative Commons Attribution 4.0 International License, which permits use, sharing, adaptation, distribution and reproduction in any medium or format, as long as you give appropriate credit to the original author(s) and the source, provide a link to the Creative Commons licence, and indicate if changes were made. The images or other third party material in this article are included in the article's Creative Commons licence, unless indicated otherwise in a credit line to the material. If material is not included in the article's Creative Commons licence and your intended use is not permitted by statutory regulation or exceeds the permitted use, you will need to obtain permission directly from the copyright holder. To view a copy of this licence, visit <http://creativecommons.org/licenses/by/4.0/>.

© The Author(s) 2023